ROYAL SOCIETY
OF CHEMISTRY

PAPER

View Article Online
View Journal | View Issue

Non-cytotoxic molybdenum-based nanostructures as effective radical scavengers†

Stefania Mura,[a] Pietro Rassu,[a] Usama Anwar,[a] Davide De Forni,[b] Barbara Poddesu,[b] Franco Lori[b] and Plinio Innocenzi (iD) *[a]

Sodium molybdate is a potential candidate as an effective antioxidant even if no significant proof of its antioxidant properties has been reported so far, especially for nanoparticles. In the present work, we have synthesised sodium molybdate nanoparticles using MoS_2 and $NaOH$ as precursors. After thermal treatment at 200 °C for 20 hours, sodium molybdate nanoparticles with an average dimension of 26 nm have been obtained. An intermediate treatment time of 8 hours gives nanoparticles with a mixed composition, MoS_2–Na_2MoO_4. The nanoparticles have been characterized using Raman and infrared spectroscopy, X-ray diffraction, atomic force microscopy and dynamic light scattering. The radical scavenging capability has been tested using 1,1-diphenyl-2-picrylhydrazyl as a molecular probe. Both pure Na_2MoO_4 and the heterostructured MoS_2–Na_2MoO_4 nanoparticles have exhibited excellent radical scavenging activity in aqueous solutions, with MoS_2–Na_2MoO_4 showing an enhanced response. Another test has been conducted in the solid state, introducing the nanoparticles within a mesoporous titania film matrix. The high photocatalytic activity of titania has been completely quenched by the presence of the sodium molybdate nanoparticles. Finally, *in vitro* studies using Hep G2 cells further confirmed the antioxidant capacity of the nanoparticles without inducing cytotoxicity. These findings suggest that sodium molybdate nanoparticles are promising candidates for biomedical and environmental applications, particularly in reducing oxidative stress.

Introduction

The pursuit of highly efficient nanosized antioxidant systems is a hot trend in research. Free radicals, including reactive oxygen species (ROS) and reactive nitrogen species (RNS), are highly reactive molecules characterized by unpaired electrons.[1] They are generated in the body through natural metabolic processes or from external sources such as radiation, pollution, and chemicals. Excessive production of free radicals can result in oxidative stress and development of several diseases, including cancer, neurodegenerative disorders (*e.g.*, Alzheimer's and Parkinson's disease), cardiovascular diseases, and aging-related conditions.[2] For these reasons, significant attention has been paid to next-generation antioxidant molecules and nanoparticles, which offer versatile tools adaptable to a variety of chemical environments. In particular, oxidant–antioxidant systems in the form of nanoparticles can exhibit enhanced performances because they have an extremely high surface area relative to their volume.[3] This property provides more active sites for interactions with free radicals, thereby increasing their efficiency in capturing and neutralizing ROS and RNS.

In this work, we have focused our attention on sodium molybdate, as a potential innovative antioxidant,[4] even if no substantial evidence of its antioxidant activity has been yet reported. In particular, to the best of our knowledge, sodium molybdate has not yet been synthesized as nanoparticles. Sodium molybdate typically crystallizes in a tetragonal system, though variations in the structure can occur depending on synthesis conditions. The Mo atom is coordinated with four oxygen atoms in a tetrahedral arrangement, forming a MoO_4^{2-} anion, which pairs with Na^+ cations.[5] These anionic and cationic interactions lead to the formation of a crystalline structure.

Experimental

Materials and methods

Molybdenum(IV) sulfide powder (MoS_2, powder, <2 μm, 99%), a dialysis bag (mol. weight cut-off 2000 Da), sodium hydroxide pellets, titanium(IV) chloride ($TiCl_4$, 99.9%), ethanol (EtOH absolute, 99.5%), Pluronic F-127 (12 600 g mol^{-1}), and stearic acid powder (97%) were purchased from

[a] *Laboratory of Materials Science and Nanotechnology (LMNT), CR-INSTM, Department of Biomedical Sciences, University of Sassari, Viale S. Pietro 43/B, 07100 Sassari, Italy. E-mail: plinio.innocenzi@uniss.it*

[b] *ViroStatics S.r.l., Viale Umberto I, 46, 07100 Sassari (SS), Italy*

† Electronic supplementary information (ESI) available. See DOI: https://doi.org/10.1039/d5lf00085h

Sigma-Aldrich, USA. Milli Q water was used during the experiments. All reagents purchased were of analytical grade and used without further purification.

Synthesis of sodium molybdate nanostructures from MoS$_2$

The synthesis of sodium molybdate nanoparticles was achieved through the integration and refinement of various methods.[6,7] In a typical procedure, MoS$_2$ powder was mixed with NaOH pellets in a 1:20 (MoS$_2$:NaOH) molar ratio and dissolved in 25 mL Milli-Q water. Once the solution stopped producing smoke, it was transferred to a 25 mL Teflon-lined autoclave that was then placed in an oven, where it was heated from 25 °C to 200 °C at a rate of 2 °C per minute. The reaction was carried out at 200 °C for either 8 or 20 hours. After the thermal treatment was completed, the heating system was turned off, allowing the sample to cool naturally to 25 °C. The product was centrifuged at varying speeds (2000, 4000, 9000, and 12 000 rpm) for 10 minutes at each speed to eliminate larger MoS$_2$ particles.

In each centrifugation step, the precipitate was discarded, and the supernatant was collected. Finally, the collected supernatant was dialyzed in 1 liter of Milli-Q water, changing the water three times while stirring, until neutrality was achieved.

Synthesis of mesoporous TiO$_2$ thin films

Mesoporous titania thin films were prepared using a template-assisted self-assembly process.[8] To start, 1.3 grams of Pluronic F-127 was dissolved in 28.8 mL of ethanol (EtOH). Subsequently, 2.2 mL of TiCl$_4$ in 18 mL of EtOH was added to this solution. After stirring for 15 minutes, 3.6 mL of Milli-Q water was added. The final molar ratio in the solution was as follows: TiCl$_4$:EtOH: Pluronic F-127:H$_2$O = 1:40:0.005:10. This mixture was then divided into two glass vials of 25 mL for different experiments. One vial solution was directly used to deposit the mesoporous titania thin films, while to the second vial, which contained 10 mL of the precursor solution, 1.35 mL of previously synthesized nanoparticles (at a concentration of 5 mg mL^{-1}) were added.

Silicon wafers served as substrates for film deposition *via* dip-coating. The silicon substrates were immersed in the titania sols for 30 seconds and then withdrawn at a rate of 100 mm min^{-1}. The relative humidity (RH) in the deposition chamber was maintained below 25% using airflow. The deposited films were first dried in air at 60 °C for 1 hour and then thermally treated at 130 °C for 2 hours and at 350 °C for 3 hours. The samples were placed in an oven at 25 °C, and then the temperature was gradually increased to 350 °C at a heating rate of 5 °C min^{-1}.

Material characterization

UV-visible spectra were recorded using a Nicolet Evolution 300 spectrophotometer (Thermo Fisher, Waltham, MA, USA) from 200 to 600 nm, employing quartz cuvettes of 1 cm light-path. The samples were measured in water at a concentration of 3 mg mL^{-1}.

Photoluminescence emission spectra were recorded on a spectrofluorometer Horiba Jobin Yvon NanoLog equipped with a 450 W xenon lamp as the excitation source. Fluorescence maps (*x*-emission; *y*-excitation; *z*-intensity, false colour scale) were collected using a 5 nm slit for excitation and emission.

Infrared spectra were obtained by using a Bruker Vertex 70 spectrophotometer in absorbance mode in the range of 4000–400 cm^{-1} at 4 cm^{-1} resolution and 256 scans, using a Si wafer (100) as a substrate. A silicon wafer was used as the background; the baseline was fitted by a concave rubber band correction with OPUS™ 7.0 software and data were analysed using ORIGIN PRO™ software.

Raman spectra of freeze-dried nanoparticles were collected in the 65–1555 cm^{-1} range with a 3–5 cm^{-1} resolution using a Senterra confocal Raman microscope (Bruker, 785 nm laser, 100 mW power, and 50× objective), irradiating the samples deposited on Si substrates. The X-ray diffraction (XRD) patterns were recorded in the angular range of 10 < 2θ < 80°, using a high-resolution Bruker Discovery 8 instrument with a copper tube CuKα (λ = 1.54056 Å). The X-ray generator worked at a power of 40 kV and 40 mA. The scan type used was the detector scan, starting at 10° and ending at 80°. The step size was 0.02° and the time per step was 0.5 s repeated until a good signal-to-noise ratio was obtained.

Spectroscopic ellipsometry (α-Wollam) with a fixed-angle geometry was used to measure the thickness and refractive index of the films, which were analysed *via* CompleteEASE 4.2 software. Three measurements were taken at different locations for each specimen and the mean value was reported. A transparent film on Si model was introduced as a fitting parameter and used to calculate the refractive index. The results of the fits were evaluated on the basis of the mean squared error, which was maintained below 10.

Atomic force microscopy (AFM) images were collected using an NT-MDT Ntegra AFM platform (Eindhoven, The Netherlands) NTEGRATING probe nanolaboratory. The surface morphology of NPs was evaluated on Si samples of 0.5 × 0.5 cm at 0.5 to 1 Hz scan speed in semicontact mode, using a silicon tip with a nominal resonance frequency of 150 kHz, 5 N m^{-1} force constant, and 10 nm typical curvature radius. Images were processed using the software Gwyddion.

The average size of the nanoparticles in solution at a concentration of 0.1 mg mL^{-1} was analysed with a particle size analyzer DLS (dynamic light scattering) Horiba LB-550.

The wettability of titania films alone and with the samples treated for 8 hours was evaluated by contact angle analysis (Dataphysics OCA 20), after the deposition of a drop of water (5 μL) on the samples and estimating the angle between an ideal horizontal plane, supporting the surface of the droplet, and the drop. The contact angle was taken as a median of at least three measurements.

DPPH modified antioxidant assay

The DPPH assay was carried out following a modified protocol based on a previously published method.[9] A 0.25 mM DPPH solution was prepared by dissolving DPPH in methanol. Different volumes of nanoparticles (ranging from 125 to 1000 μL) at a concentration of 0.3 mg mL^{-1} were diluted to a total volume of 1000 μL with Milli-Q water. To this solution, 1 mL of the 0.25 mM DPPH solution was added. The reaction mixture was then incubated in the dark at room temperature for 20 minutes. After incubation, the absorbance of the mixture was measured at a wavelength of 517 nm. A control was prepared by adding 1 mL of DPPH in methanol to 1 mL of water. This experiment was conducted for both 8 and 20 h processed samples. The radical scavenging activity (RSA) of the nanoparticles was calculated using the following formula:

$$RSA\ (\%) = (Abs\ control - Abs\ sample)/Abs\ control \times 100$$

where the Abs control is the absorbance of the DPPH radical in methanol, and the Abs sample is the absorbance of the DPPH radical in the presence of nanoparticles.

Solid state photocatalytic test

Stearic acid was selected as the molecular probe to evaluate the photocatalytic activity of the mesoporous TiO_2 film doped with sodium molybdate nanoparticles. This method has been reported in previous articles.[8,10] The changes of vibrational modes within the 2945–2845 cm^{-1} range (–CH$_2$ and –CH$_3$ stretching) were used to characterize the photodegradation of stearic acid across different samples. This process was quantified by calculating the corresponding integral of the infrared bands as a function of irradiation time.

Initially, stearic acid was dissolved in ethanol at a concentration of 3.3 mg mL^{-1}. A 100 μL aliquot of this solution was then applied to the films using spin-coating at a speed of 1500 rpm for 30 seconds. The stearic acid-coated films were irradiated with 365 nm light from a UV lamp (Spectroline, ENF-280C/FE) at a distance of 1 cm. The irradiation time was varied from 0 to 90 minutes, and the FTIR spectra of the samples were recorded immediately after illumination. The photocatalysis tests were repeated three times to ensure the reproducibility of the results.

Antioxidant activity of NPs in cells

The total antioxidant capacity (TAC) of nanoparticles (NPs) was measured in the Hep G2 cell line (hepatocellular carcinoma, ATCC HB-8065) using a commercially available colorimetric kit (Abcam ab65329). The cells were seeded in 6-well plates at a density of 1×10^6 cells per well in Dulbecco's modified Eagle medium (DMEM) (Biowest) supplemented with 1% glutamine (Biowest), 1% penicillin/streptomycin (Biowest), and 10% fetal bovine serum (FBS). The day following seeding, the cells were exposed to different concentrations of 8 h and 20 h samples, 0.15, 0.075, and 0.0375 mg mL^{-1}, for 24 hours. After the treatment, the cells were washed and then processed following the instructions provided with the kit. During the TAC assay, the Cu^{2+} ion is reduced to Cu^+ by the nanoparticles. The presence of a protein mask prevents the reduction of Cu^{2+} by proteins in the culture medium, thus allowing for the analysis of antioxidants exclusively from the nanoparticles. The reduced Cu^+ ion is then chelated with a colorimetric probe, which produces a broad absorbance peak at 570 nm, indicative of the total antioxidant capacity. A standard curve is generated using various concentrations of Trolox, and TAC is expressed as Trolox equivalents.

Cytotoxicity assessment

The cytotoxicity of NPs was determined by a standard MTS (3-(4,5-dimethylthiazol-2-yl)-5-(3-carboxymethoxyphenyl)-2-(4-sulfophenyl)-2H-tetrazolium) assay. HepG2 cells (hepatocellular carcinoma, ATCC HB-8065) were seeded at a density of 10 000 cells per well into a 96-well plate in DMEM (Biowest) supplemented with 1% glutamine (Biowest), 1% penicillin/streptomycin (Biowest) and 10% fetal bovine serum (Biowest) at 37 °C and 5% CO_2. 24 hours after seeding, the cells were treated with increasing concentrations of the NPs and cultured for additional 24 hours. At the end of the incubation period, the cytopathic effect was measured through the MTS assay (CellTiter 96® Aqueous One Solution Reagent, Promega) by reading absorbance values at 490 nm after background subtraction from control wells. Each compound was tested in duplicate wells to determine the average cell viability compared to the untreated control.

Statistical analysis

Student's t-test (two sided) was utilized to assess the presence of statistically significant differences among the studied samples in the antioxidant activity assay.

Results and discussion

The synthesis of sodium molybdate nanoparticles is a significant challenge, as conventional precipitation methods often lead to uncontrolled crystallization.[11,12] Therefore, a specifically tailored synthesis strategy is required. We have started our synthesis using MoS_2 powders as a source of molybdenum to obtain MoS_2 nanoparticles.[7] In a further step, sodium hydroxide has been added to add Na$^+$ ions in excess into the solution that finally gives, after thermal treatment, sodium molybdate nanoparticles.

Synthesis of sodium molybdate nanoparticles

The precursor source for Mo was a commercial powder of MoS_2. To exfoliate MoS_2, an ion intercalation route was used.[7,13] The powder was added to an aqueous solution of NaOH, where it completely dissociated into sodium (Na$^+$) and hydroxide ions (OH$^-$). Na$^+$ ions penetrate between the MoS_2 layers weakening the van der Waals forces and

separating the sheets.[7,14] The process was assisted by heating the mixture to 200 °C to enhance the diffusion of Na^+ ions into the MoS_2 layers and promoting the reaction with sodium to form sodium molybdate as nanoparticles.[15] NaOH can also react with the edges of MoS_2 layers, further assisting in exfoliation by creating defects and initiating layer separation and fragmentation into nanoparticles.[11] The excess of Na^+ ions is expected to facilitate the formation of sodium molybdate *via* the oxidation of molybdenum disulfide with oxygen in the presence of sodium hydroxide that is a strong base, according to the following reaction:

$$2MoS_2 + 9O_2 + 12NaOH \rightleftharpoons 2Na_2MoO_4 + 4Na_2SO_4 + 6H_2O \quad (1)$$

Molybdenum in MoS_2 is in the +4 oxidation state and is oxidized to +6 in Na_2MoO_4, while sulphur in MoS_2 is in the −2 oxidation state and is oxidized to +6 in Na_2SO_4, which is highly soluble in water. The precursor MoS_2 has a layered hexagonal crystal structure, similar to graphite,[16] with trigonal prismatic ($2H$-MoS_2) or octahedral ($1T$-MoS_2) coordination. The hexagonal structure consists of strong covalent bonding within layers and weak van der Waals interactions between layers, allowing for easy exfoliation[12] (Fig. 1). Each MoS_2 layer consists of a sandwich-like structure, S–Mo–S, where a plane of Mo atoms is sandwiched between two planes of S atoms. The Mo–S bond length is approximately 2.4 Å while the interlayer spacing is around 6.5 Å and is governed by van der Waals forces.[13] The product of MoS_2 thermally assisted exfoliation under basic conditions is also crystalline. In its most common form, $Na_2MoO_4·2H_2O$ (sodium molybdate dihydrate) has a tetragonal crystalline structure[16,17] with water molecules that stabilize the crystal structure by forming hydrogen bonds with oxygen in the MoO_4^{2-} units (Fig. 1).

The synthesis of Na_2MoO_4 nanoparticles from MoS_2 powder and NaOH pellets has been designed to employ an aqueous solution, avoiding the addition of organic solvents, which can be a source of difficult-to-handle impurities. Obtaining Na_2MoO_4 from NaOH requires a strongly basic environment, possibly with an excess of NaOH to drive the reaction forward. NaOH, as said, acts as an intercalating agent and contributes to the separation and cutting of the layers of bulk MoS_2.[18,19] Research on sodium molybdate (Na_2MoO_4) in nanosize is still in its early stages, and to date, no studies have focused specifically on this compound as nanoparticles.

The products of MoS_2 exfoliation and the reaction with NaOH have been characterized to identify their structural and optical properties. Fig. 2 displays the X-ray diffraction (XRD) patterns of MoS_2 (black line) and the reaction products following a thermal treatment for 8 (red) and 20 hours (green line). The XRD data have been collected by measuring the diffraction angle ($2\theta°$) from 10 to 60°. The diffraction pattern of MoS_2 exhibits three intense peaks at 14.4, 32.8, and 58.3°, which correspond to the (002), (100), and (110) crystal planes of MoS_2, respectively (JCPDS card 00-006-0097).[20] The diffraction peak at 14.4° is the most significant as it is the signature of the hexagonal crystalline structure with the space group $P6_3/mmc$.[21]

The XRD patterns of the samples obtained after the thermally assisted exfoliation for 8 and 20 hours show the rise of another crystalline species, which has been identified as sodium molybdate dihydrate[22] (JCPDS card 00-001-0113). The main peak at 12.8° is due to diffraction of the (020) plane and also other smaller peaks related to this species can been found (Fig. 2 inset). Na_2MoO_4 is synthesized *via* exfoliation of MoS_2 followed by its reaction with sodium hydroxide, as described in reaction (1). The selected reaction times ensure complete conversion into Na_2MoO_4. The crystallite dimension of sodium molybdate has been calculated using the Scherrer formula to be 34.6 and 30.5 nm, after 8 and 20 hours of thermal treatment at 200 °C, respectively.

After the thermal treatment at 8 and 20 hours, the pattern assigned to MoS_2 is no longer detected, as shown by the disappearance of the (002) diffraction peak at 14.4°. This result suggests that MoS_2 has reacted during the material processing.[23–25] The vanishing of the XRD pattern may be also related to a different scenario, *i.e.*, the reaction of MoS_2 with NaOH to form other species or exfoliated layers that no longer exhibit a crystalline structure.[26–28] This finding will be further clarified by FTIR and Raman spectroscopy (*vide infra*).
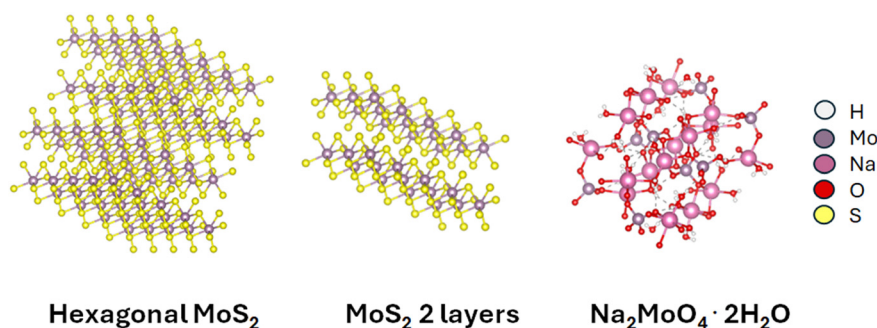

Fig. 1 The crystalline structure of MoS_2, a 2 layer structure of MoS_2 and the crystalline structure of $Na_2MoO_4·2H_2O$.
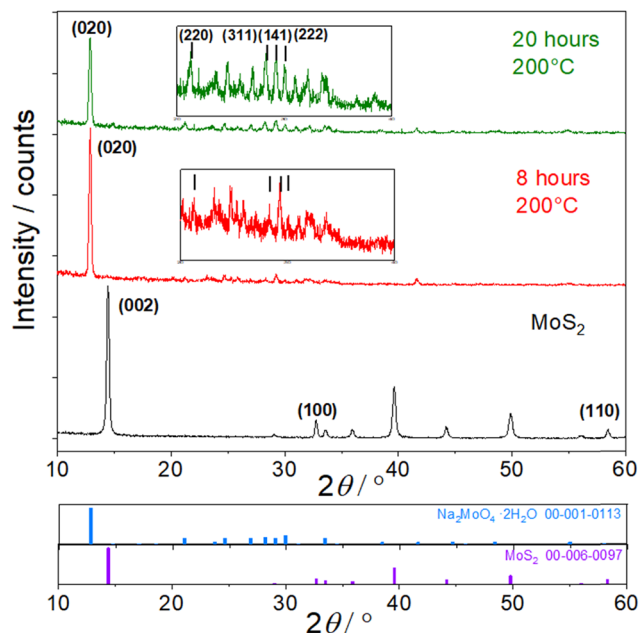
Fig. 2 XRD patterns of precursor MoS_2 (black line) and samples obtained after thermally assisted exfoliation for 8 (red line) and 20 hours (green line) at 200 °C, respectively. The inset shows a magnified view of the corresponding pattern. The bottom panel shows the standard XRD patterns of sodium molybdate dihydrate (blue) (JCPDS card 00-001-0113) and crystalline hexagonal MoS_2 (violet) (JCPDS card 00-006-0097).

Na_2MoO_4 nanoparticle structure and properties

To get a better clue of the nanostructures formed upon thermally assisted exfoliation of MoS_2 by NaOH, FTIR and Raman measurements have been performed. Fig. 3a shows the FTIR absorption spectra, in the 1300–400 cm^{-1} interval, of MoS_2 (blue line), Na_2MoO_4 (8 h) (black line) and Na_2MoO_4 (20 h) (red line).

The infrared spectrum of MoS_2 shows the characteristic absorption band, intense and narrow, at 474 cm^{-1} due to out-of-plane stretching vibration of Mo–S (A_{2u} mode). This mode involves the out-of-plane vibrations of the sulphur atoms moving symmetrically with respect to the molybdenum

atom.[29] It is a non-degenerate mode where sulphur atoms move perpendicular to the plane of the layers. The MoS_2 spectrum is also characterized in the 500–700 cm^{-1} range by several weak and narrow bands (428, 490, 519, 630, 650, 681 cm^{-1}). Zecchina et al.[30] have correlated these bands, arising from combinations and overtones of fundamental vibrational modes, with the multilayer structure of the powder, and ultimately with the structure of MoS_2 nanoparticles. The samples treated for 8 and 20 hours show triplet absorption bands located at 822, 860 and 902 cm^{-1}. They represent the signature of sodium molybdate and are assigned to MoO_4^{2-} antisymmetric stretching (v_{as}), MoO_4^{2-} symmetric stretching (v_s), and Mo=O symmetric stretching (v_s), respectively. The infrared spectra of the MoS_2 exfoliation products no longer exhibit the structured absorption bands observed in the precursor molybdenum disulfide, indicating that multilayered structures should no longer be present. On the other hand, the broadening of the Mo–S stretching mode at 474 cm^{-1} indicates that in the nanoparticles, several chemical environments form, such edges and defects. The infrared spectra of the exfoliated materials show also a very intense and broad absorption band peaking at 1125 cm^{-1} that is assigned to sulphate groups adsorbed on defect sites.[31] This is likely due to the formation of edges and defects in MoS_2 nanostructures, which are able to adsorb different chemical species, including sulphate groups.[31,32] Fig. 3b displays the infrared spectra in the O–H stretching region at high wavenumbers. The MoS_2 sample does not show any vibrational mode in this interval, while the exfoliation products have an intense and broad absorption band. Interestingly, this band is given by the overlapping of two bands, one peaking at 3292 cm^{-1} (more intense) and a second one at 3440 cm^{-1}, detected as a shoulder. The first one is assigned to O–H stretching of adsorbed water and the second one to O–H stretching in Mo–OH defective and edge sites. The breaking of the Mo–S–Mo bonds during the exfoliation induces the formation of Mo–OH terminal groups.[33,34]

We have coupled the infrared analysis with Raman measurements that should give more details about the nanoparticle structure. Fig. 4 shows the Raman spectra of the
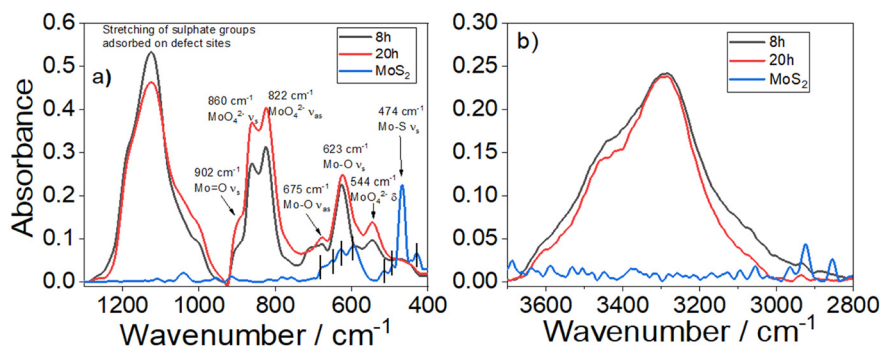

Fig. 3 a) FTIR absorption spectra, in the 1300–400 cm^{-1} range, of MoS_2 (blue line) and Na_2MoO_4 (20 h) (red line) and Na_2MoO_4 (8 h) (black line) exfoliated products. The weak and narrow bands detected at lower wavelengths are indicated by a black segment. b) FTIR absorption spectra, in the 3750–2800 cm^{-1} range.
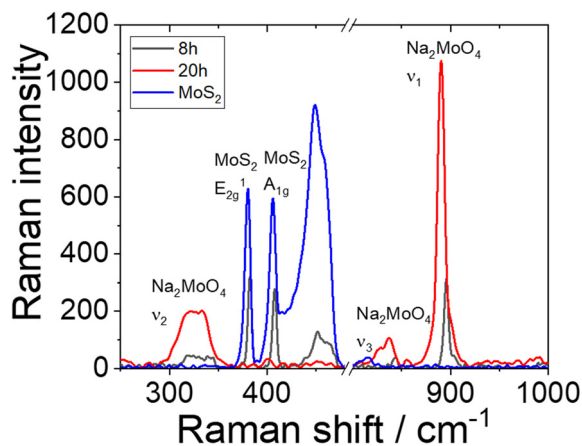
Fig. 4 Raman spectra of MoS_2 (blue line) and reaction products Na_2MoO_4 (8 h) (black line) and Na_2MoO_4 (20 h) (red line) at 200 °C. Laser excitation wavelength: $\lambda = 785$ nm.

MoS_2 powder (red line) and the reaction products after 8 (black line) and 20 hours (blue line) of exfoliation. The Raman spectrum of MoS_2 has two characteristic signals due to the in-plane (E_{2g}^1) mode at 380 cm^{-1} and the out-of-plane (A_{1g}) mode at 405 cm^{-1}, which corresponds to the optical phonon mode.[35] The out-of-plane mode is due to the vibration of the S atom, and the in-plane mode is a mixed atom vibration of Mo–S bonds on the opposite directions.[21,35]

In the reacted samples, the MoS_2 signal is detected only in the sample treated for 8 hours. Interestingly, the XRD data, however, do not show any diffraction pattern due to crystalline MoS_2. At longer reaction times, the modes due to MoS_2 disappear and only the spectrum of Na_2MoO_4 is observed. The Raman spectra of sodium molybdate are characterized by four modes: at 890 cm^{-1}, symmetric stretching of the Mo–O bonds in the MoO_4^{2-} tetrahedral unit (v_1), at 837 cm^{-1}, asymmetric stretching of the Mo–O bonds (v_3), and at 326 cm^{-1}, symmetric bending (or deformation) of the O–Mo–O bonds (v_2).[36] The signal at 450 cm^{-1} is due to the resonance mode.[37,38] The Raman spectra, in agreement with the FTIR finding, indicate that after 8 hours of reaction of MoS_2 with NaOH, the Na_2MoO_4 nanoparticles should contain some residuals of MoS_2 likely as small layered fragments.[39] At the longest time of reaction, instead, the MoS_2 precursor has been completely transformed into Na_2MoO_4. In general, the relative positions of the E_{2g}^1 and A_{1g} modes can give a good indication of the number of MoS_2 layers.[40] The two modes in the bulk are detected at 380 and 406 cm^{-1} ($\Delta = 26$ cm^{-1}), while those in the Na_2MoO_4 (8 h) sample at 382 and 407 ($\Delta = 25$ cm^{-1}), which indicates that the MoS_2 should be present as small fragments of several layers.[9,41]

The hydrodynamic diameter of Na_2MoO_4 (8 h) (Fig. 5a) has an average size distribution of 23 nm, while in Na_2MoO_4 (20 h) (Fig. 5b) it is 26.3 nm, in agreement with the results obtained by XRD. In particular, the AFM images
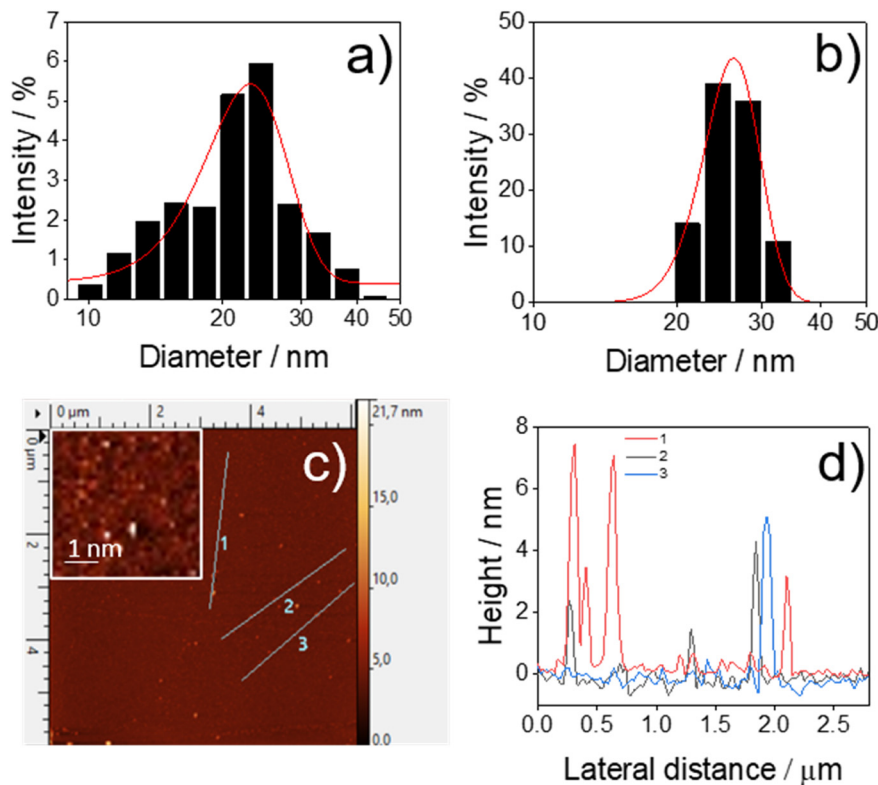

Fig. 5 Dynamic light scattering of the exfoliated samples after a) 8 h and b) 20 h thermally assisted exfoliation. The red line is a guide for the eyes. c) AFM image of the Na_2MoO_4 (8 h) nanoparticles. The inset shows a magnified view of the NPs. d) Dimensional profiles of the nanoparticles; the curves correspond to the lines 1, 2 and 3 in c).
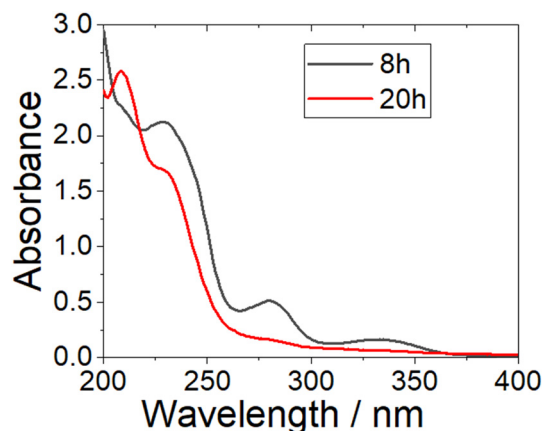
Fig. 6 UV-vis absorption spectra of Na$_2$MoO$_4$ (8 h) (black line) and Na$_2$MoO$_4$ (20 h) (red line) aqueous dispersions (concentration of 3 mg mL^{-1}).

(Fig. 5c and d) of Na$_2$MoO$_4$ (8 h) show the presence of nanoparticles of a few nanometers. The theoretical single layer of MoS$_2$ has a thickness of 0.6–1 nm,[42,43] thus, the results indicate that molybdenum disulfide is present as a fragment of a few layers.

Fig. 6 shows the UV-vis absorption spectra of aqueous dispersions of Na$_2$MoO$_4$ (8 h) (black line) and Na$_2$MoO$_4$ (20 h) (red line). The UV spectra are very informative and strongly supportive of the previous findings. In particular, Na$_2$MoO$_4$ (20 h) shows the typical signature of sodium molybdate in aqueous solution that is characterized by an absorption band at 210 nm with an overlapped shoulder at 230 nm of lower intensity. The UV-vis spectrum is attributed to molybdate ions [MoO$_4$]$^{2-}$ that are the only molybdenum species detected.[44] In contrast, Na$_2$MoO$_4$ (8 h), besides the absorption bands of the molybdate ions, shows other two additional absorption bands at longer wavelengths: 280 nm and 330 nm.[45] The 280 nm band is assigned to the excitonic properties of MoS$_2$ nanostructures[46] and the 340 nm band to the direct transition from the deep valence band to the conduction band.[47] Interestingly, the original hexagonal crystalline structure or 2D MoS$_2$ with large lateral dimensions should display four peaks at 340 nm, 430 nm, 590 nm, and 650 nm as characteristic absorption bands, but besides the

340 nm signal, they are not detected.[48,49] This result well supports the finding that a few layered MoS$_2$ fragments of small dimensions form the nanostructures.

Fig. 7 shows the fluorescence map of the aqueous dispersion of the Na$_2$MoO$_4$ (8 h) (Fig. 7a) and Na$_2$MoO$_4$ (20 h) samples (Fig. 7b). Na$_2$MoO$_4$ (8 h) shows only very weak fluorescence. The fluorescence increases in intensity in the Na$_2$MoO$_4$ (20 h) nanoparticles that exhibit a broad emission in the blue-green spectral range (~350–500 nm), peaking at λ_{ex} = 264 nm and λ_{em} = 395 nm. The origin of this fluorescence, clearly observed only in the Na$_2$MoO$_4$ (20 h) sample, possibly arises from the electronic transitions of molybdate (MoO$_4$$^{2-}$) anions.[50] The fluorescence is primarily due to charge transfer transitions within the MoO$_4$$^{2-}$ groups, specifically the ligand-to-metal charge transfer from oxygen to molybdenum.[51]

DPPH antioxidant assay

The sodium molybdate nanoparticles have been used for a specific antioxidant assay using 1,1-diphenyl 2-picrylhydrazyl (˙DPPH) as a molecular probe. ˙DPPH is a free radical that has high stability in the powder form and is used to evaluate the capacity of different molecules to act as free radical scavengers. The antioxidant assay is based on the evaluation of the decrease of the 517 nm absorption band in a ˙DPPH solution after adding an antioxidant. A change in colour from deep violet to yellow is observed when the free radical is scavenged.[52] The reaction between ˙DPPH and antioxidant H-A is:

$$(\text{˙DPPH}) + (\text{H-A}) \rightarrow \text{DPPH-H} + (\text{A˙}) \qquad (2)$$

The antioxidant reacts with ˙DPPH that is reduced to DPPH-H causing a decrease in the absorbance (Fig. 8). The UV-vis spectra of aqueous dispersions of Na$_2$MoO$_4$ (8 h) and Na$_2$MoO$_4$ (20 h) in the presence of ˙DPPH show that the best antioxidant activity is displayed by Na$_2$MoO$_4$ (8 h) (Fig. 8a); at the highest concentration, 0.15 mg mL^{-1}, the dispersion turns yellow. The dispersion containing Na$_2$MoO$_4$ (20 h) shows a very similar trend (Fig. 8b), even if the antiradical activity is less effective (in average around 10%) compared to
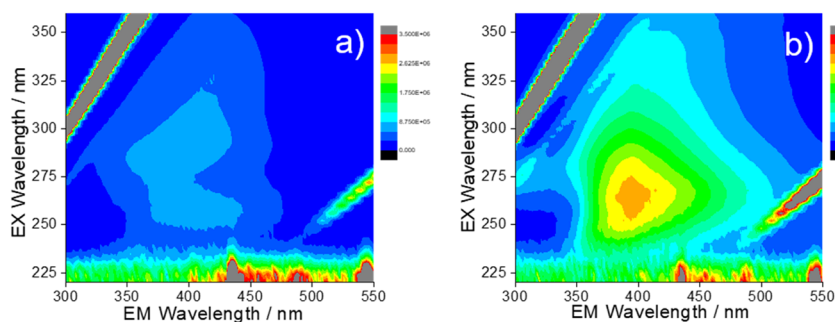

Fig. 7 Fluorescence map (*x*-emission, *y*-excitation, *z*-intensity on the false colour scale) of Na$_2$MoO$_4$ (8 h) (a) and Na$_2$MoO$_4$ (20 h) (b) treated samples.
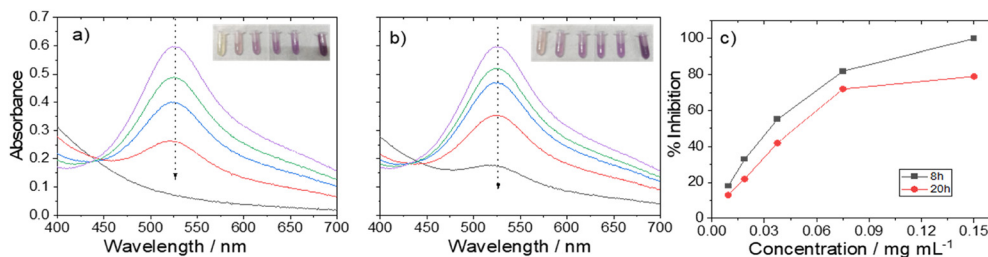
Fig. 8 DPPH assay. UV-vis spectra after the addition of the aqueous solutions of nanoparticles to DPPH solution in MeOH with a final concentration of 0.15 (black line), 0.075 (red line), 0.0375 (blue line) and 0.01875 mg mL^{-1} (green line). The violet line is the DPPH used as a control. a) Na$_2$MoO$_4$ (8 h) samples and b) Na$_2$MoO$_4$ (20 h) samples. The insets in a and b show the snapshots of the solutions at increasing nanoparticle concentrations from right to left. The arrows indicate the direction of the decrease in absorbance with the increase of nanoparticles in solution. c) Antioxidant activity measured by the DPPH assay for the two samples. The lines are a guide for the eyes.

the Na$_2$MoO$_4$ (8 h) sample (Fig. 8c). On the other hand, bulk MoS$_2$ does not show any antioxidant property and the solution remains dark violet.

The DPPH tests give two important findings: the first result is the antioxidant activity exhibited by the sodium molybdate nanoparticles, and the second one is the synergic effect on radical scavenging given by the formation of a MoS$_2$–Na$_2$MoO$_4$ heterostructure that shows a better antioxidant activity in comparison with pure Na$_2$MoO$_4$ nanoparticles. The previous experimental results suggest that the samples thermally exfoliated with a shorter processing time form nanoparticles with the MoS$_2$–Na$_2$MoO$_4$ heterostructure, containing small fragments of residual MoS$_2$ embedded within the Na$_2$MoO$_4$ matrix. This finding is supported by XRD that shows no crystalline MoS$_2$ present in the sample. Additionally, the possibility that the system consists of separated sodium molybdate nanoparticles and small amorphous fragments of molybdenum disulfide can be ruled out, as the final product has been purified and all small residues have been removed. The spectroscopic data, including infrared, Raman, and UV-visible analyses, further support the formation of a heterostructure by demonstrating specific properties that can only be explained through the formation of a nanocomposite.

Sodium molybdate (Na$_2$MoO$_4$) contains Mo(VI) species, which can undergo redox cycling (Mo^{6+} $\leftrightarrow$ Mo^{4+}) to continuously facilitate electron transfer. The mechanism of the antioxidant activity is, therefore, attributed to the Mo^{6+}/Mo^{4+} ion couple and Mo, with its three oxidation states (+4, +5, +6) being able to participate in different redox reactions.[53] Mo is found in catalytic centers of different enzymes where it is involved as a catalyst for redox and oxygen transfer reactions.[54] In recent studies, Na$_2$MoO$_4$ has been used as an antioxidant nanomaterial to reduce the damage due to ROS.[34,55] Examples of the antioxidant capacity of sodium molybdate to treat different pathologies related to oxidative stress have been also widely reported in the literature.[56–58] The possibility of using these nanosystems as efficient ROS scavengers, also under physiological conditions, opens the way to possible biological and pharmaceutical applications for the treatment of osteoarthritis caused by oxidative stress,[59] for the treatment of amyloid-related diseases such as

Alzheimer's disease[60] or for bioimaging,[61] due to their fluorescence properties.

The antioxidant activity of these nanomaterials arises from the formation of a Na$_2$MoO$_4$–MoS$_2$ heterostructure. Molybdenum disulfide, in fact, is a layered transition metal dichalcogenide with excellent electron mobility, enabling it to act as an electron donor and acceptor, efficiently transferring electrons to neutralize ROS.[62] While MoS$_2$ is a semiconductor with a narrow bandgap ($\sim$1.2–1.8 eV), Na$_2$MoO$_4$ is an ionic compound that influences charge dynamics at the interface.[63] In a heterostructure, charge separation is more efficient, reducing the electron–hole recombination rate and making electron donation to ROS more effective. This leads to a stronger ability to neutralize radicals like superoxide (O$_2^{\cdot-}$) and hydroxyl radicals ($^{\cdot}$OH).[64] This synergistic redox interplay allows for a faster and more efficient ROS scavenging process compared to individual components.

Antioxidant test in the solid state

We have also evaluated the antioxidant activity of sodium molybdate nanoparticles in the solid state. A mesoporous titania matrix in the form of a thin film has been used for the experiment. Titania is a semiconducting material characterized by strong photocatalytic activity when excited by ultraviolet light.[65] In the mesoporous form, the high surface area and pore order that promote the diffusion of radical species into the matrix amplify the photocatalytic activity.[66] The photocatalysis of titania is mainly related to the formation of radical species,[67] so the incorporation of nanoparticles that function as radical scavengers into the matrix should reduce or quench the photocatalysis of titania.

In particular, the photocatalytic activity of titania is observed in the anatase phase, which in sol–gel films forms at around 300 °C, while the full crystallization to anatase is observed at around 450 °C.[65] The choice of the thermal treatment for the present application of mesoporous titania films needs to be carefully designed. The thermal processing, in fact, should remove the block copolymer template, avoiding, at the same time, the pore collapse and
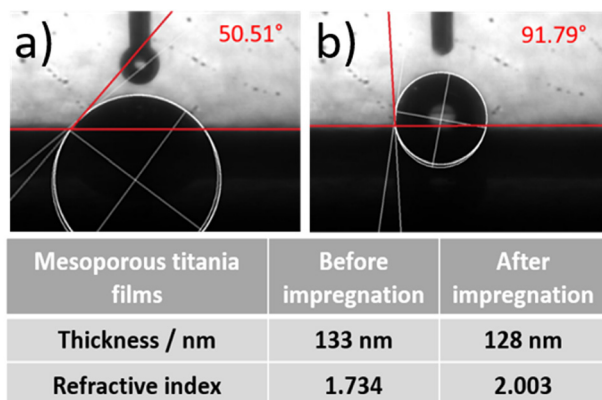
© 2025 The Author(s). Published by the Royal Society of Chemistry

Fig. 9 Contact angles of mesoporous titania films, before (a) and after impregnation with Na_2MoO_4 (8 h) NPs (b). The table lists the thickness and refractive index before and after impregnation with the nanoparticles.

allowing the crystallization of the titania into anatase. A treatment at 350 °C represents the best compromise; the XRD data (Fig. S1†) show crystallization of the films into titania anatase.

Doping the films by impregnation does not produce a significant variation in the thickness but changes the surface contact angle and the refractive index (Fig. 9); this increase is due to the doping with the nanoparticles. These changes are a direct result of the successful doping with the nanoparticles of the mesoporous films.

Several techniques have been explored for incorporating sodium molybdate and MoS_2 nanoparticles into mesoporous titania films. One method is the one-pot technique, which involves directly adding the nanoparticles into the precursor sol. This resulting sol is then used to deposit mesoporous titania films through dip-coating, utilizing a supramolecular templating agent as a mold of the mesopore structure. Another technique that has been tested is post-impregnation, where pre-formed mesoporous films are immersed in a solution containing the nanoparticles. Additionally, a third approach combines both the one-pot and post-impregnation techniques in a sequential manner. The data in Fig. 10 show the results of the tests performed on mesoporous titania films obtained by the one-pot method. Among all approaches tested, this method yielded the highest performance.

The photocatalysis test on mesoporous titania films has been performed using a procedure we have applied in previous work, whereby a solution of stearic acid is deposited on the film in a controlled manner.[8] Then the sample is exposed to UV light for different times and the degradation of stearic acid is assessed by infrared spectroscopy. Using stearic acid as an indicator, compared to other options like dyes such as rhodamine B, offers the advantage of providing insights into the actual removal of the molecule from the surface. This method focuses on the effective photochemical degradation of the molecule, rather than just the degradation of optical properties, which may not necessarily correlate with the molecule removal.
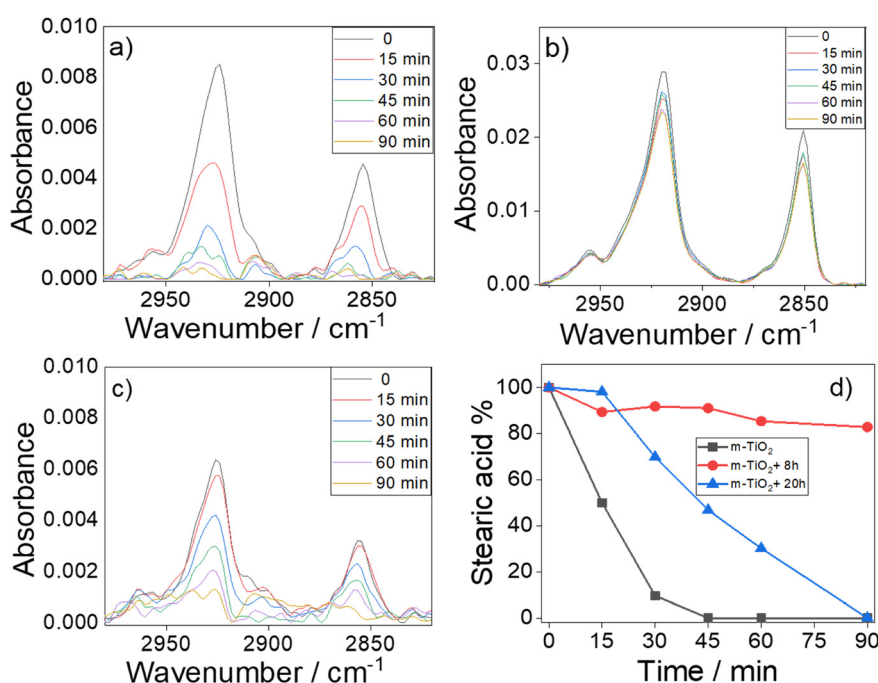

Fig. 10 FTIR absorption spectra at different exposure times to UV light of stearic acid deposited on mesoporous titania films. (a) Mesoporous titania (m-TiO$_2$) films as a reference; b) mesoporous titania films doped with Na_2MoO_4 (8 h) nanoparticles (m-TiO$_2$ + Na_2MoO_4 (8 h)); (c) mesoporous titania films doped with Na_2MoO_4 (20 h) nanoparticles (m-TiO$_2$ + Na_2MoO_4 (20 h)). d) Photoinduced degradation of stearic acid (%) as a function of time in m-TiO$_2$ (black squares), m-TiO$_2$ + Na_2MoO_4 (8 h) (red circles) and m-TiO$_2$ + Na_2MoO_4 (20 h) (blue triangles). The lines are a guide for the eyes.

© 2025 The Author(s). Published by the Royal Society of Chemistry

RSC Appl. Interfaces, 2025, **2**, 1299–1310 | **1307**

Fig. 10a shows the variation in intensity of the two infrared bands in the 2945–2845 cm^{-1} range, corresponding to the vibrational modes of the –CH$_2$ and –CH$_3$ groups of stearic acid, as a function of UV exposure time on mesoporous titania films. After 45 minutes, the photocatalytic removal of stearic acid from the surface is complete, in agreement with previous studies. In contrast, when the material is doped *via* impregnation with Na$_2$MoO$_4$ (8 h) nanoparticles, a diametrically opposite behaviour is observed. Stearic acid is only minimally degraded, with a reduction of about 10% (Fig. 10b), and the photocatalytic activity of titania is inhibited by the presence of sodium molybdate and MoS$_2$ nanoparticles. An intermediate result is obtained by impregnating titania films with Na$_2$MoO$_4$ (20 h) NPs (Fig. 10c) that partially inhibit the photocatalytic activity of titania, leading to the complete removal of stearic acid after 90 minutes.

The degradation rate of stearic acid (%) has been evaluated by integrating the corresponding infrared absorption bands, using eqn (3):

$$\text{Stearic acid (\%)} = I_t/I_0 \times 100 \qquad (3)$$

where I_t is the integral value at time t and I_0 is the initial value at t = 0. The degradation of stearic acid has been plotted as a function of UV exposure time (Fig. 10d).

Antioxidant activity in cells

The antioxidant activity of sodium molybdate nanoparticles has been evaluated in Hep G2 cells using a commercially available assay kit (Abcam ab65329). The cells have been exposed to different concentrations of Na$_2$MoO$_4$ (8 h) and Na$_2$MoO$_4$ (20 h) nanoparticles for 24 hours, specifically at concentrations of 0.15, 0.075, and 0.0375 mg mL^{-1}, based on the results of the DPPH antioxidant assay. This assay measures the ability of a compound to reduce Cu^{2+} ions to Cu$^+$ ions, which are then chelated with a colorimetric probe that produces a broad absorbance band peaking at 570 nm.
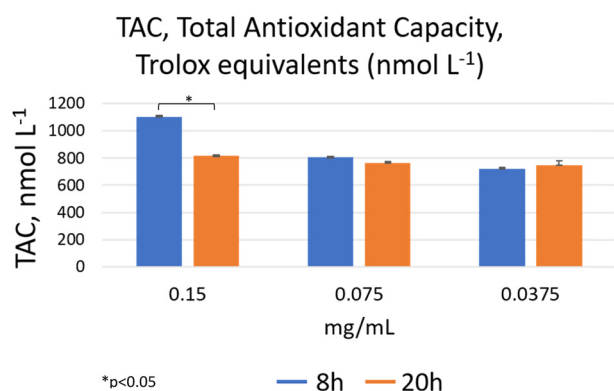

Fig. 11 Total antioxidant capacity of Na$_2$MoO$_4$ (8 h) (blue) and Na$_2$MoO$_4$ (20 h) (orange) at 0.15, 0.075 and 0.0375 mg mL^{-1} in Hep G2 cells expressed as Trolox equivalents.
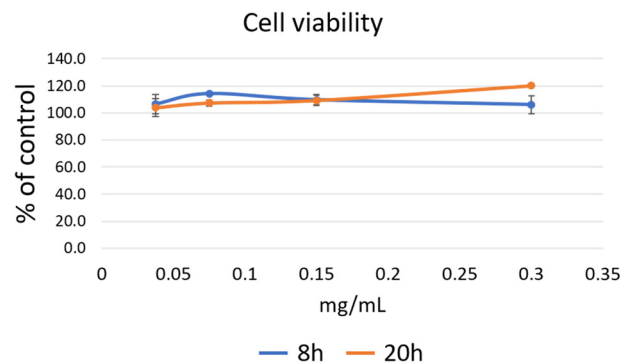

Fig. 12 Cytotoxicity of Na$_2$MoO$_4$ (8 h) (blue) and Na$_2$MoO$_4$ (20 h) (orange) to Hep G2 cells evaluated through a standard MTS assay. The lines are a guide for the eyes.

This absorbance is proportional to the total antioxidant capacity (TAC) when compared to the standard antioxidant compound, Trolox. Fig. 11 shows the average TAC data for the nanoparticles.

The *in vitro* results closely reflect the antioxidant activity of the nanoparticles as assessed by the DPPH assay. The antioxidant activity of Na$_2$MoO$_4$ (8 h) was significantly higher than that of Na$_2$MoO$_4$ (20 h) at 0.15 mg mL^{-1}. The cytotoxicity of NPs has been assessed in parallel in Hep G2 cells using a standard MTS assay. Fig. 12 shows the average cell viability values of NPs at the different concentrations, expressed as the percentage of the untreated control. The concentrations of nanoparticles demonstrating antioxidant activity did not induce cytotoxic effects in HepG2 cells.

Conclusions

Thermally assisted exfoliation of MoS$_2$ with NaOH has been demonstrated to be a very effective route to obtain sodium molybdate nanoparticles. The synthesis has been based on thermally assisted exfoliation of MoS$_2$ at 200 °C for controlled reaction times. The time of processing is a critical synthesis parameter. In fact, the samples processed for 20 hours transform into pure sodium molybdate nanoparticles, while after 8 hours nanocomposite particles with a MoS$_2$–Na$_2$MoO$_4$ heterostructure form. Structural characterization confirmed the transformation of MoS$_2$ into sodium molybdate, with XRD, FTIR, Raman, and UV-vis analyses providing clear evidence of the structure and properties of the nanoparticles.

The resulting nanoparticles have exhibited excellent radical scavenging activity, making them strong candidates for antioxidant applications. Moreover, the presence of MoS$_2$ in the Na$_2$MoO$_4$ heterostructure enhanced the antioxidant effect due to multiple oxidation states, facilitating redox reactions. The antioxidant properties have also been explored by preparing a nanocomposite consisting of sodium molybdate nanoparticles embedded in mesoporous titania films. Tests involving the degradation of stearic acid under UV light demonstrated that the incorporation of the nanoparticles completely quenched the oxidant activity of the

1308 | *RSC Appl. Interfaces*, 2025, **2**, 1299–1310

© 2025 The Author(s). Published by the Royal Society of Chemistry

mesoporous titania films. Additionally, *in vitro* tests using Hep G2 cells confirmed the antioxidant capacity of these nanoparticles while showing no cytotoxic effects at effective concentrations.

The antioxidant tests have shown that the sodium molybdate nanoparticles have an excellent radical scavenging activity besides being non-cytotoxic and are, therefore, good candidates as nanomaterials for being applied to reduce the oxidative stress in biological systems. Sodium molybdate nanoparticles have been untested in 3D hydrogel or polymer scaffolds and their tissue regeneration capability would be important to assess as a next step. Future studies will pave the way for the application of molybdenum-based nanostructures in areas like oxidative stress-related disease treatment, tissue engineering, and advanced antioxidant coatings.

Data availability

The data will be made available to a public repository and are also available upon request to the corresponding author.

Author contributions

Dr. Stefania Mura: conceptualization, data curation, formal analysis, investigation, methodology, software, validation, visualization, writing – original draft, writing – review and editing. Pietro Rassu: data curation, formal analysis, contact angle measurements and contribution to the graphical abstract. Usama Anwar: formal DLS analysis. Davide De Forni, Barbara Poddesu, Franco Lori: biological assays of antioxidant activity and data analysis. Prof. Plinio Innocenzi: conceptualization, data curation, funding acquisition, investigation, project administration, resources, supervision, validation, visualization, writing – original draft, writing – review and editing.

Conflicts of interest

The authors declare no conflicts of interest.

Acknowledgements

References

1 H. Sies, V. V. Belousov and N. S. Chandel, *et al.*, *Nat. Rev. Mol. Cell Biol.*, 2022, **23**, 499–515.

2 A. Pinna, L. Malfatti, G. Galleri, R. Manetti, S. Cossu, G. Rocchitta, R. Migheli, P. A. Serra and P. Innocenzi, *RSC Adv.*, 2015, **5**, 20432–20439.

3 A. Pinna, E. Cali, G. Kerherve, G. Galleri, M. Maggini, P. Innocenzi and L. Malfatti, *Nanoscale Adv.*, 2020, **2**, 2387.

4 S. R. Panneerselvam and S. Govindasamy, *Clin. Chim. Acta*, 2004, **345**, 93–98.

5 K. Matsumoto, A. Kobayashi and Y. Sasaki, *Bull. Chem. Soc. Jpn.*, 1975, **48**, 1009–1013.

6 Q. Liu, C. Hu and X. Wang, *RSC Adv.*, 2016, **6**, 25605–25610.

7 M. N. Pallikkarathodi and C. Jobin, *Bull. Mater. Sci.*, 2022, **45**, 184.

8 J. Ren, L. Stagi, L. Malfatti, V. Paolucci, C. Cantalini, S. Garroni, M. Mureddu and P. Innocenzi, *Nanomaterials*, 2022, **12**, 1074.

9 O. P. Sharma and T. K. Bhat, *Food Chem.*, 2009, **113**, 1202–1205.

10 S. Alofi, C. O'Rourke and A. Mills, *J. Photochem. Photobiol., A*, 2023, **435**, 114273.

11 Y. Liu, X. Zou, D. Duan, L. Luo, S. Chen and L. Zhong, *J. Cryst. Growth*, 2019, **506**, 102–107.

12 J. Casas and J. Lagos, *Chem. Ind. Chem. Eng. Q.*, 2020, **26**, 17.

13 L. Ali, F. Subhan, M. Ayaz, S. S. Hassan, C. C. Byeon, J. S. Kim and S. Bungau, *Nanomaterials*, 2022, **12**, 3465.

14 P. R. Wu, Z. Liu and Z. L. Cheng, *Mater. Lett.*, 2019, **248**, 236–240.

15 R. Kalt, A. Arcifa, C. Wäckerlin and A. Stemmer, *Nanoscale*, 2023, **15**, 46–57.

16 S. Miyake and M. Wang, *Nanoscale Res. Lett.*, 2015, **10**, 123.

17 F. Capitelli, M. Selim and K. M. Kalyan, *Asian J. Chem.*, 2006, **18**, 2856–2860.

18 K. C. Lalithambika, K. Shanmugapriya and S. Sriram, *Appl. Phys. A: Mater. Sci. Process.*, 2019, **125**, 817.

19 A. Abareshi, M. Arshadi Pirlar and M. Houshiar, *Mater. Res. Express*, 2019, **6**, 105050.

20 K. C. Lalithambika, K. Shanmugapriya and S. Sriram, *Appl. Phys. A: Mater. Sci. Process.*, 2019, **125**, 817.

21 S. J. Panchu, K. Raju, H. C. Swart, B. Chokkalingam, M. Maaza, M. Henini and M. K. Moodley, *ACS Omega*, 2021, **6**, 4542–4550.

22 F. Zhang, C. Liu, S. Chandrasekar, Y. Li and F. Xu, *Int. J. Miner., Metall. Mater.*, 2024, **31**, 91–105.

23 Q. Liu, C. Hu and X. Wang, *RSC Adv.*, 2016, **6**, 25605–25610.

24 H. Dong, S. Tang, Y. Hao, H. Yu, W. Dai, G. Zhao, Y. Cao, H. Lu, X. Zhang and H. Ju, *ACS Appl. Mater. Interfaces*, 2016, **8**, 3107–3114.

25 B. Sathyan, A. M. Tomy, N. PM and J. Cyriac, *RSC Adv.*, 2023, **13**, 14614–14624.

© 2025 The Author(s). Published by the Royal Society of Chemistry

RSC Appl. Interfaces, 2025, **2**, 1299–1310 | **1309**

26 L. Chen, S. L. Hsieh, C. H. Kuo, S. Hsieh, W. H. Chen, C. W. Chen and C. Di Dong, *RSC Adv.*, 2020, **10**, 31794–31799.

27 W. Dai, H. Dong, B. Fugetsu, Y. Cao, H. Lu, X. Ma and X. Zhang, *Small*, 2015, **11**, 4158–4164.

28 M. Takase, P. K. Essandoh and R. Kipkoech, *Discov. Sustain.*, 2021, **2**, 5.

29 D. Saha and P. Kruse, *J. Electrochem. Soc.*, 2020, **167**, 126517.

30 L. Muscuso, S. Cravanzola, F. Cesano, D. Scarano and A. Zecchina, *J. Phys. Chem. C*, 2015, **119**, 3791–3801.

31 F. Maugé, J. Lamotte, N. S. Nesterenko, O. Manoilova and A. A. Tsyganenko, *Catal. Today*, 2001, **70**, 271–284.

32 Y. Xu, L. Yan, X. Li and H. Xu, *Sci. Rep.*, 2019, **9**, 2931.

33 N. Pallikkarathodi Mani and J. Cyriac, *Bull. Mater. Sci.*, 2022, **45**, 184.

34 A. Thomas and K. B. Jinesh, *ACS Omega*, 2022, **7**, 6531–6538.

35 A. Molina-Sánchez, K. Hummer and L. Wirtz, *Surf. Sci. Rep.*, 2015, **70**, 554–586.

36 S. Chatterjee, S. Barik and R. N. Choudhary, *J. Mater. Sci.: Mater. Electron.*, 2013, **24**, 3359–3364.

37 G. D. Saraiva, W. Paraguassu, M. Maczka, P. Freire, F. Sousa and J. Filho, *J. Raman Spectrosc.*, 2011, **42**, 1114–1119.

38 K. Gołasa, M. Grzeszczyk, K. P. Korona, R. Bożek, J. Binder, J. Szczytko, A. Wysmołek and A. Babiński, *Acta Phys. Pol. A*, 2013, **124**, 849–851.

39 G. D. Saraiva, C. Luz-Lima, P. T. C. Freire, A. J. Ramiro De Castro, G. P. De Sousa, F. E. A. Melo, J. H. Silva and J. Mendes Filho, *J. Mol. Struct.*, 2013, **1033**, 154–161.

40 C. Lee, H. Yan, L. E. Brus, T. F. Heinz, J. Hone and S. Ryu, *ACS Nano*, 2010, **25**, 2695–2700.

41 Y. Zhan, Z. Liu, Q. Liu, D. Huang, Y. Wei, Y. Hu, X. Lian and C. Hu, *New J. Chem.*, 2017, **41**, 3930–3938.

42 Y. Sun, W. He, X. Sun and B. Liu, *Luminescence*, 2020, **35**, 1416–1423.

43 P. C. H. Mitchell, *Speciation of molybdenum compounds in water Ultraviolet spectra and REACH read across Report for the International Molybdenum Association REACH Molybdenum Consortium*, 2009.

44 S. Ghayeb Zamharir, R. Karimzadeh and S. H. Aboutalebi, *Appl. Phys. A: Mater. Sci. Process.*, 2018, **124**, 692.

45 H. D. Ha, D. J. Han, J. S. Choi, M. Park and T. S. Seo, *Small*, 2014, **10**, 3858–3862.

46 M. Mahdavi, S. Kimiagar and F. Abrinaei, *Crystals*, 2020, **10**, 164.

47 Y. Xu, L. Yan, X. Li and H. Xu, *Sci. Rep.*, 2019, **9**, 2931.

48 L. Ali, F. Subhan, M. Ayaz, S. S. u. Hassan, C. C. Byeon, J. S. Kim and S. Bungau, *Nanomaterials*, 2022, **12**, 3465.

49 Y. Sun, W. He, X. Sun and B. Liu, *Luminescence*, 2020, **35**, 1416–1423.

50 Y. Hizhnyi, S. Nedilko, V. Chornii, T. Nikolaenko, K. Terebilenko and R. Boiko, *Solid State Phenom.*, 2013, **200**, 114–122.

51 M. H. Chisholm, S. E. Brown-Xu and T. F. Spilker, *Acc. Chem. Res.*, 2015, **17**, 877–885.

52 O. P. Sharma and T. K. Bhat, *Food Chem.*, 2009, **113**, 1202–1205.

53 Y. Yu, L. Lu, Q. Yang, A. Zupanic, Q. Xu and L. Jiang, *ACS Appl. Nano Mater.*, 2021, **4**, 7523–7537.

54 R. Hille, J. Hall and P. Basu, *Chem. Rev.*, 2014, **114**, 3963–4038.

55 P. H. Lin, Y. T. Huang and F. W. Lin, *ECS J. Solid State Sci. Technol.*, 2017, **6**, 3113–3116.

56 N. V. Perkhulyn, B. M. Rovenko, O. V. Lushchak, J. M. Storey, K. B. Storey and V. I. Lushchak, *Redox Rep.*, 2017, **22**, 137–146.

57 S. R. Panneerselvam and S. Govindasamy, *Clin. Chim. Acta*, 2004, **345**, 93–98.

58 D. Ni, D. Jiang, C. J. Kutyreff, J. Lai, Y. Yan, T. E. Barnhart, B. Yu, H. J. Im, L. Kang, S. Y. Cho, Z. Liu, P. Huang, J. W. Engle and W. Cai, *Nat. Commun.*, 2018, **9**, 5421.

59 T. Chen, H. Zou, X. Wu, C. Liu, B. Situ, L. Zheng and G. Yang, *ACS Appl. Mater. Interfaces*, 2018, **10**, 12453–12462.

60 X. Shao, C. Yan, C. Wang, C. Wang, Y. Cao, Y. Zhou, P. Guan, X. Hu, W. Zhu and S. Ding, *Nanoscale Adv.*, 2022, **21**, 46–80.

61 T. Liu and Z. Liu, *Adv. Healthcare Mater.*, 2018, **7**, 1701158.

62 Y. Yu, L. Lu, Q. Yang, A. Zupanic, Q. Xu and L. Jiang, *ACS Appl. Nano Mater.*, 2021, **4**, 7523–7537.

63 Y. Zhang, R. Zhang, Y. Guo, Y. Li and K. Li, *J. Alloys Compd.*, 2024, **998**, 174916.

64 X. Dou, Q. Zhang, S. N. A. Shah, M. Khan, K. Uchiyama and J. M. Lin, *Chem. Sci.*, 2018, **10**, 497–500.

65 N. Farooq, P. Kallem, Z. Rehman, M. I. Khan, R. K. Gupta, T. Tahseen, Z. Mushtaq, N. Ejaz and A. Shanableh, *J. King Saud Univ. - Sci.*, 2024, **36**, 103210.

66 D. Wang, L. Zhao, D. Song, J. Qiu, F. Kong and L. H. Guo, *RSC Adv.*, 2019, **9**, 29429–29432.

67 D. Carboni, D. Marongiu, P. Rassu, A. Pinna, H. Amenitsch, M. Casula, A. Marcelli, G. Cibin, P. Falcaro, L. Malfatti and P. Innocenzi, *J. Phys. Chem. C*, 2014, **118**, 12000–12009.